

Microhydraulic electrowetting actuators

Jakub Kedzierski, Kevin Meng, Todd Thorsen, Rafmag Cabrera, and Shaun Berry

Massachusetts Institute of Technology Lincoln Laboratory, Lexington, MA 02420, USA

Distribution A: Public Release

The conversion of electrical to mechanical power on a sub-centimeter scale is a key technology in many microsystems and energy harvesting devices. In this paper we present a type of capacitive energy conversion device that uses capillary pressure and electrowetting to reversibly convert electrical power to hydraulic power. These microhydraulic actuators use high surface – to – volume ratio to deliver high power at a relatively low voltage, with an energy conversion efficiency of over 65%. The pressure generated by capillary effects grows linearly with shrinking capillary diameter, as does the frequency of actuation. We present the pressure, frequency, and power scaling properties of these actuators and demonstrate that power density scales up as the inverse capillary diameter squared, leading to high efficiency actuators with strength density exceeding biological muscle. Two potential applications for microhydraulics are also demonstrated: soft-microrobotics and energy harvesting.

The conversion of electrical to mechanical power and vice versa is one of the key technologies that make the modern world possible. On a macroscopic scale, inductive motors and generators are ubiquitous as sources of both motion and electricity. They start our cars, convert steam energy to electricity in power plants, open doors, and power escalators. They work so well, and are so efficient, that on a scale above a couple of centimeters, other non-inductive forms of electrical actuation are hard to find.

However, below the 1 cm scale, inductive motors become much less efficient because the resistance of the conducting coil dominates¹. At 2 grams the maximum practical motor efficiency is 50% and falls quickly to 5% at 0.5 grams². Low efficiency is one of the reasons that microsystems such as digital light processors³, inkjet printers⁴, and microrobots⁵ tend to use other forms of actuation. The alternatives can be widely divided into resistive and capacitive actuators, based on the primary impedance mode. Some examples of resistive actuators are thermal inkjet printers, electro-osmotic pumps⁶, and shape memory alloys⁷. While very versatile, resistive actuators also tend to have low efficiency, as a large portion of power is lost as heat. Capacitive actuators, such as piezoelectrics⁸, MEMs comb-drives⁹, and electrowetting pumps¹⁰, work well on a microscale. They can be scaled to micron sizes without losing efficiency, but their actuation voltages tend to be high. For example bimorph piezoelectric actuators used in microrobotics often use voltages between 150-300V^{11,12}. While using high-voltages in a microsystem is possible with modern voltage converters¹² it leads to additional inefficiencies and system complexity that is best to be avoided. Increasing voltage in a capacitive actuator is an effective way to increase power because capacitor energy is $\frac{1}{2}CV^2$. However an alternative way to increase power is to increase the capacitance per unit volume. This strategy is already used in energy storage where large surface-to-volume ratio capacitors, such as electrolytic and super-capacitors, are employed. In an electrolytic capacitor a rough or porous metal with a high surface area forms one electrode, and the other is formed by a conductive fluid - an electrolyte that fills in all the pores. When considering how to design high capacitance actuators we took this example and focused on fluidic capacitive actuation effects. It turns out that electrowetting^{13,14} is well suited for building high capacitance actuators with a large surface to volume ratio. Electrowetting, which is already widely used with planar capacitors, changes the effective surface energy of a fluid-solid interface in response to an applied voltage. Surfaces can transition reversibly from hydrophobic to hydrophilic because the

surface energy between the conducting fluid and the solid surface changes as $-C_a V_a^2/2$. Where C_a is the areal capacitance of the dielectric, and V_a is the applied voltage between the solid electrode and the conducting fluid.

In this paper we describe how to use electrowetting in high surface-to-volume geometries to build powerful and scalable microhydraulic actuators. We will show how these actuators improve in pressure, frequency, and power with reduced capillary diameter and demonstrate high efficiencies of over 60% in electrical to hydraulic power conversion. We will also demonstrate how these actuators can be used as drivers for soft microrobotics, or in reverse to harvest energy¹⁵, converting hydraulic power to electrical power.

Before considering the behavior of electrowetting actuators with complex geometries, it is important to understand the behavior of planar electrowetting actuators¹⁰. Such an actuator is shown in Fig. 1. Two of its important characteristics are γ_{wo} , the surface tension between the fluid phases, and h , the separation between the two plates. Since the surfaces are hydrophobic under zero voltage, a certain pressure is required to push water into the actuator. This pressure, P_{\max} is $2\gamma_{wo}/h$. Under typical operation the pressure generated by the actuator is $P_{\max}/2$. Note that changing h does not change the hydraulic energy delivered per cycle, because reducing h increases pressure but reduces volume actuated, and increasing h does the opposite. In planar electrowetting actuators this sets a limit on the actuator power. To compare output power, we will use S_d , the strength density, calculated as the power delivered by the actuator divided by its volume. A typical planar electrowetting pump¹⁰ has an S_d of only 30 nW/ μ L, considering the thickness of the substrate and typical frequencies of operation. This is inadequate for most applications, and significantly below the power density of biological muscle, which has an S_d of 1 mW/ μ L¹⁶.

In order to break the tradeoff between pressure and volume we consider more complex geometries with high surface-to-volume ratios. Three of these geometries are shown in Fig. 2, all of which give higher capacitance than planar capacitors, or conversely offer a smaller capillary diameter and therefore higher pressure, at the same volume. In this paper we will describe the behavior of multichannel plates shown in Fig. 2a, and porous actuators Fig. 2c. Microhydraulic actuation in a first-order multichannel plate has already been demonstrated by pioneering work of Prins et. al.¹⁷, however the authors do not evaluate their power density, efficiency, energy harvesting or demonstrate the scaling properties. They do predict that smaller capillary diameters will lead to higher pressure and greater power. We demonstrate this trend for the first time by building several multichannel plates with various capillary diameters and evaluating their properties.

The multichannel plates tested in this experiment are shown in Fig. 3, the testing and fabrication methodology is described in the methods section. Fig. 4 shows the response of the 25 μ m capillary diameter multichannel plate to triangular voltage waves of two different frequencies. Actuation proceeds in a similar way to Fig. 1, with h replaced by the capillary diameter D . The governing equations ignoring inertial effects are¹⁰:

$$Q = P_s/R_s \quad (1)$$

$$P_s = P_b - \Delta P \quad (2)$$

$$\Delta P = P_{\max} - 2C_a V_a^2/D \quad (3)$$

$$P_{\max} = 4\gamma_{wo}/D \quad (4)$$

Here Q is the flow rate, P_s is the driving pressure, R_s is the total system hydraulic resistance, P_b is the back pressure applied to the water phase, ΔP is the pressure difference across the water/oil interface, P_{\max} is the pressure required to push water into the capillaries at $V_a = 0$, D is the capillary diameter, γ_{wo} is the water/oil surface tension, C_a is the capacitance per unit area, and V_a is the applied voltage. At 2 Hz actuation proceeds in the following way: starting at time zero the channels are filled with decane because $P_b < \Delta P$, and actuator displacement is zero. At V_a of ~ 14 V ΔP becomes smaller than P_b and the

actuator channels begin to fill with water. The speed of the fill increases with time as P_s increases with increasing V_a . Actuation stops once the actuator is full of water due to the capillary stop at the end of the channel, as described in the methods section. The condition where water bleeds completely through the actuator can occur if V_a is too high, and the capillary stop does not work. On the falling side of the triangle wave, once V_a is below 14V, ΔP increases above P_b driving water out of the actuator. During retraction P_s is negative, accelerating the retraction as ΔP increases. A similar actuation occurs when the negative peak of the voltage waveform causes ΔP to fall below P_b , hence two actuations per voltage cycle. The current waveform is shown in Fig. 4b, the actuator charges quickly as actuation occurs and then discharges during retraction. The complex nature of the current waveform can be understood by integrating it to obtain the charge waveform and dividing that by the voltage waveform. The result is the capacitance of the actuator as a function of time shown in Fig. 4a, and corresponds with the fluid displacement seen by the camera. Thus we can conclude that the current waveform is simply the actuator charging and discharging while its capacitance is changing due to actuation. The capacitance values of 10 nF, unactuated, and 78 nF, fully actuated, match those expected from the geometry of the actuator. The electric and hydraulic powers are shown in Fig. 4c, electric power input is calculated as the current waveform, I_a , multiplied by the voltage waveform, V_a , and the hydraulic power output is calculated as the driving pressure, P_s , times the measured flow rate, Q . Note that electrical power is positive as the actuator is charged, and becomes negative as the actuator discharges; this means that during retraction the actuator returns unused energy back to the power supply. The hydraulic power delivered is always positive because it takes work to move fluid through the system in either direction. When the integrated hydraulic power output is divided by the integrated electrical power input, the actuator efficiency can be obtained. We obtained 68% and 66% efficiency at 4 Hz and 40 Hz, respectively. This is considerably higher than for piezoelectric actuators¹⁸ and any form of resistive actuation we are aware of. At 40 Hz, Fig. 4d-f, the actuator is being driven near its maximum speed. There is a significant inertial phase delay between the voltage-squared waveform and the displacement of the actuator. At this speed inertial effects of the fluid in the system become a significant factor in the actuation. It takes time to accelerate and decelerate the fluid causing the displacement waveform to lag behind the voltage-squared waveform.

Shrinking the capillary diameter should increase the pressure, capacitance, and power density of the microhydraulic actuators. In order to examine scaling, we fabricated two multichannel plates with different capillary diameters, 150 μm and 25 μm , but similar capillary aspect ratios (L/D) of ~ 5 and ~ 8 respectively, Fig. 3. Each plate was loaded with a total hydraulic system resistance, R_s (sPa/ μL), in proportion to the hydraulic resistance of the actuator, R_a , with $R_a/R_s \sim 1/7$. Maximum power delivered to the load occurs at $R_a/R_s = 1/2$, but a lower impedance fraction ($F_R = R_a/R_s$) results in a smaller fraction of the hydraulic power being dissipated in the actuator itself. For exact loading configuration and testing protocol see the methods section. Plates were tested to determine driving pressure, P_s , and hydraulic power density, S_d , at f_{max} , the frequency that gives the maximum power output. The scaling trends are shown in Fig. 5, S_d scales as $1/D^2$, when F_R and L/D are held constant, because both of its components, pressure and frequency, scale as $1/D$. According to these trends it is possible to make microhydraulic actuators stronger than biological muscle at capillary diameters below 6 μm .

To understand why strength density scales so quickly as the capillary diameter shrinks, let's consider each component separately. Pressure is $P_{\text{max}} = 4\gamma_{wo}/D$ and scales as $1/D$. The measured driving pressure P_s was observed to be lower than $P_{\text{max}}/2$ at maximum frequency, but it still scaled proportionally to P_{max} as $1/D$, see Fig. 5a. The reduction of P_s below $P_{\text{max}}/2$ may occur because actuation was done with a triangle wave and the voltage is below its maximum for most of the waveform. The second component of strength density, frequency f_{max} , is a bit more complex. The scaling trend for the hydraulic resistance of the multichannel plate is:

$$R_a = \frac{128(L+4D)\mu_{eff}}{\pi D^4 N} \quad (5)$$

With μ_{eff} being the effective viscosity, N the total number of channels, L the channel length, and D the channel diameter. In the numerator L is modified by $4D$ to help account for pipe exit and entrance losses. System loading is proportional so $R_s \propto R_a$. Since $N \propto D^{-2}$, and $L \propto D$, due to the fixed aspect ratio, R_s scales as $1/D$. Given that R_s and P_s both scale as $1/D$, the flow Q is constant. Frequency is the inverse time per cycle or $f_{\text{max}} = Q/2V_D$, where V_D is the volume actuated. V_D scales as D , as the length of the channels shrinks in proportion to D . This gives f_{max} scaling of $1/D$. Measured and expected frequency trends are shown in Fig. 5b, measurements confirm the $1/D$ frequency scaling. The fluid actuated reduces proportionally to D when scaling, because the volume of the actuator is shrinking. Increasing volume at the same capillary diameter and aspect ratio can be done by adding channels (N), although eventually the plate geometry becomes very thin and it is better to use higher order plates, Fig. 2b. When calculating f_{max} in Fig. 5, inertial effects were not considered, for a model including inertial effects see the supplemental section. In this system, inertial effects can be described by an inertial time constant τ_c , and limit the frequency to $\sim 1/\tau_c$. The mass of the fluid inside the channels themselves is not significant as shown by the $1/\tau_c$ inertial self-limit in Fig. 5b. However, if a sufficiently large amount of mass needs to be actuated outside the actuator, inertial effects can become significant. Fig. 5b shows some approximate $1/\tau_c$ limits imposed on frequency by inertial effects, for 1 mm and 5 mm long hydraulic water links outside the actuator, where for this calculation R_s is set to the hydraulic resistance of such links. As expected smaller systems have higher inertial limits. Fig. 5c shows the hydraulic power delivered per unit volume of the actuator, S_d . Predicted values of S_d in Fig. 5c are proportional to the product of pressure and frequency, until D is very small and thus S_d scales as $1/D^2$. Measurements of the hydraulic power for the two multichannel plates confirm this trend. We were able to increase the strength density of the actuator from $2.1 \mu\text{W}/\mu\text{L}$ at $D = 150 \mu\text{m}$ to $44 \mu\text{W}/\mu\text{L}$ at $D = 25 \mu\text{m}$, just by scaling. Extrapolating the scaling trends gives an S_d of $100 \text{ mW}/\mu\text{L}$ at $D = 300 \text{ nm}$; this is 100 times stronger than biological muscle.

There is a limit to S_d scaling. The electrical energy delivered to the actuator must be capacitively stored within a dielectric which has a finite breakdown field. The fluoropolymers currently used in electrowetting actually have a low maximum operational electric field of about 0.1 V/nm^{19} . This sets a dielectric minimum thickness of $T_d = 200 \text{ nm}$ when using V_a of 20 V and γ_{wo} of 50 mJ/m^2 , as was done in this paper. The additional actuator volume produced by the non-scaling dielectric thickness causes the S_d trend in Fig. 5c to deviate from $1/D^2$, as D approaches T_d . With higher electric breakdown field electrowetting materials this limit can be increased. The model for S_d is:

$$S_d = \frac{\gamma_{wo}^2 D^2 F_p^2 F_R F_V}{2\mu_{\text{eff}} L(L+4D)(D+2T_d)^2} \quad (6)$$

Here F_p (pressure fraction) is defined as $F_p = P_s/P_{\text{max}}$, F_R (impedance fraction) as $F_R = R_a/R_s$, and F_V (volume fraction) as $F_V = V_{\text{used}}/V_{\text{act}}$. V_{used} is the volume of the actuator composed of the actuated fluid and corresponding dielectric, and V_{act} is the total volume of the actuator. The inverse capillary aspect ratio D/L , the oil-water surface tension, and pressure fraction have quadratic influence on S_d , while viscosity μ_{eff} , impedance fraction, and volume fraction have a linear influence. Inertial effects reduce S_d in a complex way not reflected by this relation, by lowering the operational frequency, f_{max} .

One potential application of microhydraulic actuators is soft microrobotics. In soft robotics, elastic components are deformed by inflating their internal reservoirs, either hydraulically or pneumatically²⁰. Since our microhydraulic actuators are compact sources of hydraulic power, they can be used to actuate soft microrobotic components. We demonstrate the operation of a soft robotic hinge driven by a $25 \mu\text{m}$ D actuator plate, as shown in Fig. 6. The hinge, fabricated completely from elastic polydimethylsiloxane (PDMS), consists of an elastic reservoir that can be hydraulically expanded. The asymmetry in the top and bottom membranes of the reservoir causes the hinge to bend as the internal reservoir expands. Refer to the Supplemental Section for fabrication and testing details. With the actuator off, the water-filled elastic reservoir in the hinge provides the back pressure P_b to the microhydraulic actuator. When the system is actuated, the microhydraulic actuator fills with water, emptying the reservoir and resulting in deformation at the rotational hinge joint. In turn, the strain mismatch between the compliant topside and rigid underside of the joint generates a net torque that

rotates the straight segment of the hinge. Fig 6 shows the microrobotic system response to a triangle voltage wave, of 28 V amplitude and 3.8 Hz frequency at mechanical resonance. Fig. 6a and 6b show the hinge at maximum and minimum deflections with the actuator off and on respectively. Fig. 6c shows the COMSOL simulation of the hinge at 4 kPa reservoir pressure. The hinge experiment resulted in a sustained reversible angular displacement of 28 degrees at 7.6 Hz, giving a tip deflection of 5.16 mm. Note that the actuator itself, with a total volume smaller than a 2x2x2 mm cube, is much smaller than the soft robotic hinge,. The dynamic response of the hinge-actuator system is presented in Fig. 6d. The actuation frequency falls within the range of insect wingbeat frequencies found in nature, which span from 5 Hz for *Papilio* butterflies to over 1 kHz for the *Forcipomyia* midge^{21,22}. By modulating the actuation voltage and therefore the pressure, the angular displacement can be controlled to enable intermediate displacements. The hinge-actuator configuration can be further designed to provide thrust for efficient biolocomotion, enabling long-range micro air or undersea vehicles.

Another application for the microhydraulic actuators is energy harvesting. Electrowetting has already been recognized as an excellent technique for energy harvesting¹⁵. Microhydraulic actuators described above can be configured in reverse to harvest energy. Fig. 7 shows the energy harvesting from pressure variations, with a bias voltage of 10 V, using the 25 μm D plate. By increasing capacitance through a large surface area, our devices offer similar advantages for energy harvesting as they do for actuation. The areal capacitance of the 25 μm D plate is 195 nF/cm², which is over an order of magnitude higher than the areal capacitance demonstrated by Krupenkin et al.¹⁵ using planar capacitors. The high capacitance allows the use of lower voltage during energy harvesting, as well as potentially using the water/decane system instead of a liquid metal, simplifying fabrication and reducing toxicity.

Individual microhydraulic actuators can be arrayed in series and parallel configurations. Series connections are particularly interesting as they should allow for pressure contributions from each actuator stage to add to a larger total pressure generated, helping to overcome the inertial limits. Also since surface tension has a quadratic impact on S_d , it may be possible to build microhydraulic actuators based on a liquid-metal/oil system^{15,23} that are 100 times more powerful, for the same D, as the ones presented here. In the future, these actuators can be combined with soft deformable materials or small solid hydraulic components to design powerful, scalable, and versatile systems for micro-positioning, micro-robotics, artificial muscle, and energy harvesting.

Acknowledgements

The authors thank Ingrid Guha, Richa Batra, and Prof. Berhouz Abedian for their valuable contributions, and Wei-Lin Hu and Tony Soares for their help in building the electrical test setup. This work was supported in part by the U.S. Air Force under Contract No. FA8721-05-C002. Opinions, interpretations, conclusion, and recommendations are those of the authors and not necessarily endorsed by the United States Government.

KEYWORDS: Microhydraulics, microfluidics, actuator, energy conversion, electrowetting, electrocapillary, porous materials, microsystems, soft robotics, microrobotics, energy harvesting, PDMS

References

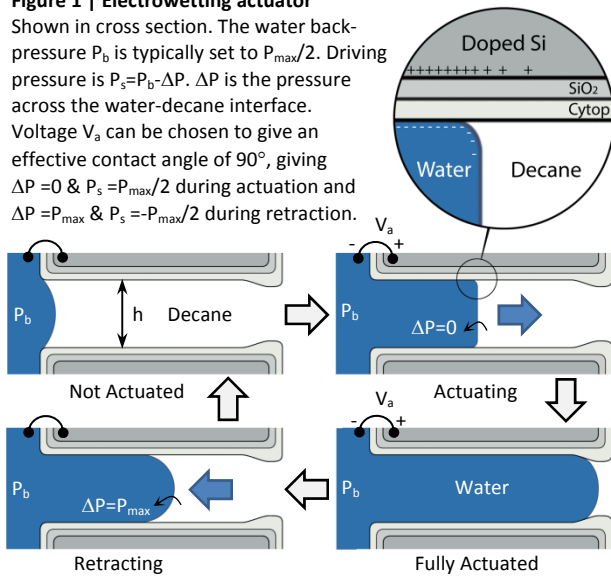
1. Laithwaite, E. R., The goodness of a machine, *Electronics and Power*, 11, 101-103 (1965).
2. Harrington, A. and Kroninger, C. M., Characterization of small dc brushed and brushless motors, ARL Tech Report ARL-TR-6389 (2013).
3. Hornbeck, L. J., Projection displays and MEMs: timely convergence for a bright future, *Proc. SPIE*, 2641, (1995).
4. Le, H. P., Progress and trends in ink-jet printing technology, *Journal of imaging science and technology*, 14, 49-62 (1998).
5. Breguet, J.M., Johansson, S., Driesen, W. & Urban, S., A review on actuation principles for few cubic millimeter sized mobile micro-robots, *Proc. 10th internat. conf. on new actuators*, 374-381 (2006).
6. Jiang, L. et al., Closed-loop electroosmotic microchannel cooling system for VLSI circuits, *IEEE Trans. on Comp. and Pack. Tech.*, 25, 347-355 (2002).
7. Nespoli, A., Besseghini, S., Pittaccio, S., Villa, E., Viscuso, S., The high potential of shape memory alloys in developing miniature mechanical devices: a review on shape memory alloy mini-actuators, *Sensors and Actuators A: Physical*, 158, 149-160 (2010).
8. Muralt, P., Ferroelectric thin films for micro-sensors and actuators: a review, *J. of Microelectromech. Microeng.*, 10, 136-146 (2000).
9. Legtenberg, R., Groeneveld, A. W., & Elwenspoek M., Comb-drive actuators for large displacements, *J. Microelectromech.*, 6, 320-329 (1996).
10. Kedzierski, J., Berry, S., & Behrouz, A., New generation of microfluidic devices, *J. of Microelectromech.*, 18, 845-851 (2009).
11. Wood, R.J., Liftoff of a 60 mg flapping-wing MAV, *IEEE/RSJ Int. Conf. on Intelligent Robots and Systems*, 1889-1894 (2007).
12. Karpelson, M., Wei, G.Y., & Wood, R., Driving high voltage piezoelectric actuators in microrobotic applications, *Sensors and Actuators: A*, (2012).
13. Zhao, Y.P., & Wang, Y., Fundamentals and applications of electrowetting: A critical review, *Rev. Adhesion Adhesives*, 1, 114-172 (2013).
14. Berry, S., Kedzierski, J. & Abedian, B. Low voltage electrowetting using thin fluoropolymer films, *J. Colloid Interface Sci.*, 303, 517-524 (2006).
15. Krupenkin, T. & Taylor, J.A. Reverse electrowetting as a new approach to high-power energy harvesting. *Nat. Commun.* 2:448 doi: 10.1038 / ncomms1454 (2011).
16. Pennycuik, C.J., & Rezende, M. A., The specific power output of aerobic muscle, related to the power density of mitochondria, *J. Exp. Biology*, 108, 377-392 (1984).
17. Prins, M. W. J., Welters, W. J. J., & Weekamp, J. W., Fluid Control in Multichannel Structures by Electrocapillary Pressure, *Science*, 291, 277-280 (2001).
18. Wang, Q.M., Du, X.H., Xu, B. & Cross, L.E., Electromechanical Coupling and Output Efficiency of Piezoelectric Bending Actuators, *IEEE Trans. on Ultrasonics, Ferroelectrics, and Frequency Control*, 46, 638-646 (1999).
19. Kedzierski, J. & Berry, S., Engineering the electrocapillary behavior of electrolyte droplets on thin fluoropolymer films, *Langmuir*, 22, 5690-5696 (2006).
20. A. Marchese, R. Katzschmann & D. Rus, A Recipe for Soft Fluidic Elastomer Robots, *Soft Robotics*, 2, 7-25 (2015).
21. Betts C. R., Wootton R. J. Wing shape and flight behaviour in butterflies (Lepidoptera: Papilionoidea and Hesperioidea): a preliminary analysis, *J. Exp. Biol.* 138, 271-288 (1988).

22. O. Sotavalta, Recordings of High Wing-Stroke and Thoracic Vibration Frequency in Some Midges, *Biological Bulletin*, 104, 439 (1953).

23. Liu, T., Sen, P., & Kim, C.J., Characterization of nontoxic liquid-metal alloy galinstan for applications in microdevices, *J. of Microelectromech.*, 21, 443-450 (2012).

Figure 1 | Electrowetting actuator

Shown in cross section. The water back-pressure P_b is typically set to $P_{max}/2$. Driving pressure is $P_s = P_b - \Delta P$. ΔP is the pressure across the water-decane interface. Voltage V_a can be chosen to give an effective contact angle of 90° , giving $\Delta P = 0$ & $P_s = P_{max}/2$ during actuation and $\Delta P = P_{max}$ & $P_s = -P_{max}/2$ during retraction.



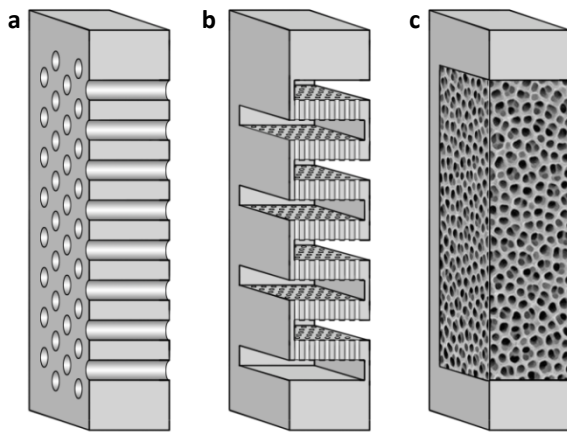


Figure 2 | Microhydraulic actuator geometries

Various high surface-to-volume geometries for microhydraulic actuators. (a) Shows a first order multichannel plate, (b) a second order multichannel plate, and (c) a porous plate. Unlike a planar capacitors, these structures can increase in volume without reduction of capillary pressure.

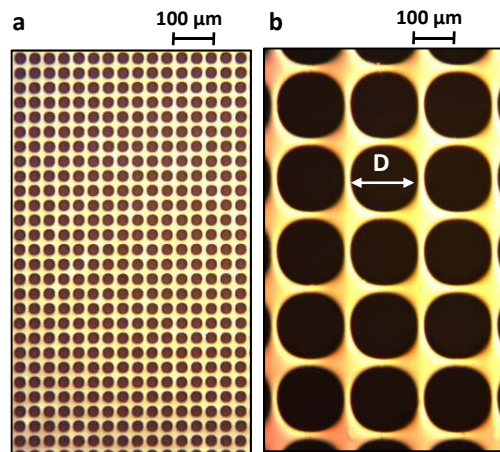


Figure 3 | Microhydraulic actuators

Two multichannel plates were tested in this experiment. (a) Top-down optical view of a plate with a capillary diameter, D , of 25 μm and a capillary length, L , of 200 μm, and (b) a plate with a D of 150 μm and L of 750 μm, under the same magnification. Plates are made from a doped silicon wafer with holes etched through the wafer.

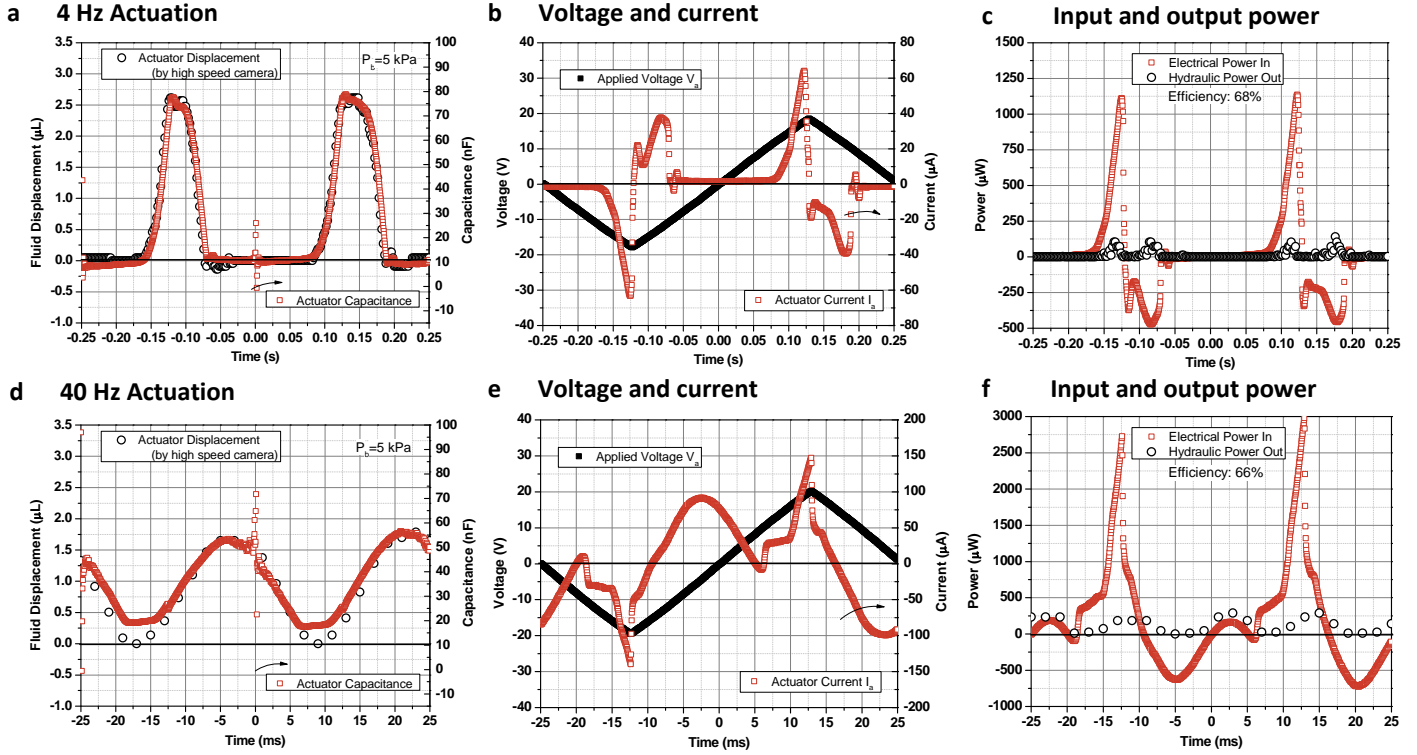


Figure 4 | Actuator electrical and hydraulic behavior

The hydraulic and electrical behavior of the $25 \mu\text{m}$ D plate when driven by a triangular voltage wave (V_a). Two different frequencies were used: a 2 Hz waveform (a-c) and a 20 Hz waveform (d-f). Actuation frequency is double the waveform frequency because actuation occurs for both the negative and positive peaks of the waveform. (a, d) Show the mechanical displacement of the fluid in the measurement tube for two actuation cycles, as well as the capacitance between the actuator and the water phase, as calculated from the voltage (V_a) and current (I_a) behavior (b, e). Because the capacitance is $\int I_a dt / V_a$, it has a singularity whenever V_a is zero, but otherwise matches the observed fluid displacement. Input and output power are shown in (c, f); the electrical power input is calculated as $I_a V_a$ and the hydraulic power output as $Q P_t$. Note that the electrical power input is negative when the actuator returns unused capacitive energy to the supply during retraction. Overall electrical to mechanical power conversion efficiency is 68% and 66%. Also note that at the higher frequency the displacement waveform (d) lags the voltage waveform (e) with actuation peaks at -4 and 21 ms that are significantly offset from the corresponding voltage-squared peaks at -12.5 and 12.5 ms.

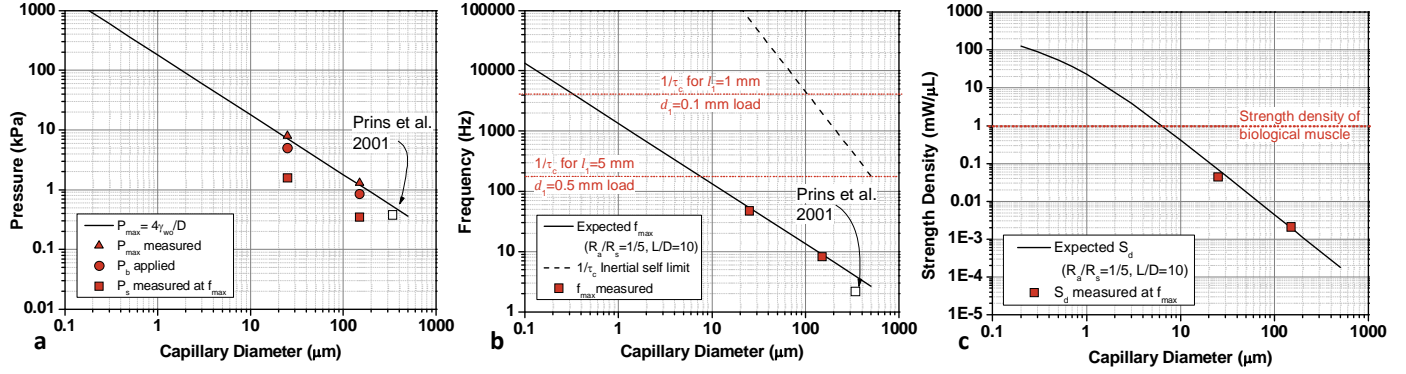


Figure 5 | Scaling

Scaling of pressure, frequency, and power density (S_d) as a function of capillary diameter, D . Measured values are shown as marks, predicted trends are shown with lines. (a) Shows pressure trends, with measured and predicted P_{max} and P_s scaling as $1/D$. (b) Shows frequency trends, with measured and predicted f_{max} . Frequency scales as $1/D$. Also shown is the inertial self-limit $1/\tau_c$, calculated using $R_s=R_aN$, $d_i=D$, $l_i=L$, and $\rho_l=1$ g/cm³, see Supplemental Section. Red lines indicate the inertial limits for two external load lines of different sizes. (c) Shows the strength density, S_d , measured for both of the multichannel plates at f_{max} , and predicted by Eqn. 6, with: $\gamma_{ow}=45$ mJ/m², $\mu_{eff}=0.001$ sPa, $F_p=1/3$, $F_R=1/5$, $F_V=1/3$, $L/D=10$, and $T_d=0.1$ μm. Until D approaches the dielectric thickness or inertial effects become significant, S_d scales as $1/D^2$, exceeding the strength of biological muscle (1 mW/μL) at values of D below 6 μm. Extracted values from Prins et al.¹⁷ are shown for reference (a,b).

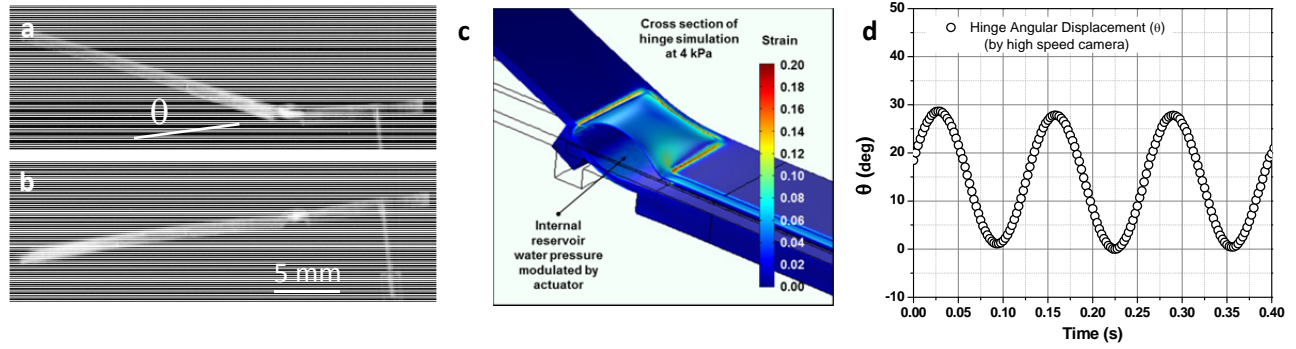


Figure 6 | Soft Microrobotics

Soft microrobotic system response to a triangle voltage wave, of 28 V amplitude and 3.8 Hz frequency at mechanical resonance of 7.6 Hz. System consists of a soft hinge made from polydimethylsiloxane hydraulically connected to a 25 μm D microhydraulic actuator, Fig 3a. (a) and (b) show the bent and unbent positions of the hinge occurring at unactuated and actuated sections of the input waveform, respectively. The hinge is deflected when the actuator is at zero volts because at that point the pressure P_b in the internal hinge reservoir is the highest. When activated, the microhydraulic actuator pulls water out of the hinge reservoir and into itself, lowering P_b and moving the hinge to an unbent position. (c) shows the steady-state COMSOL simulation of hinge angular deflection with the color scale indicating the strain in the PDMS, reservoir pressure in simulation is 4 kPa. (d) shows the measured dynamic response of the hinge angular deflection.

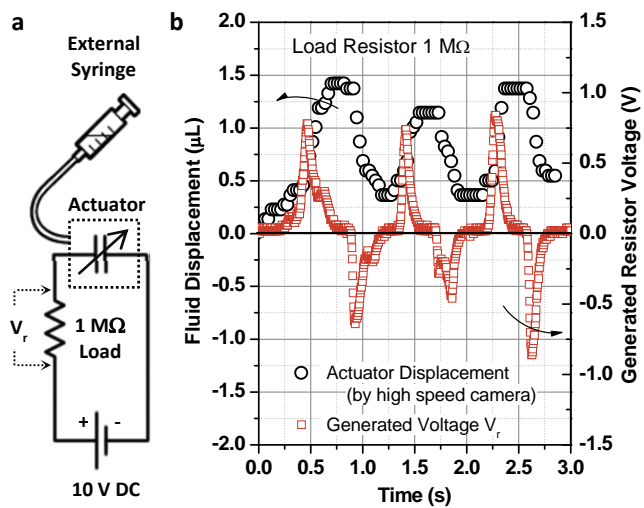


Figure 7 | Energy Harvesting

(a) Electronic configuration for energy harvesting. Voltage is kept constant at 10 V. Fluid is actuated with an external syringe. The change in actuator capacitance produces current and voltage in the load resistor. (b) Measured actuator fluid displacement and generated resistor voltage. Syringe was manually operated at $\sim 1\text{ Hz}$.